

## Convectively Unstable Anti-Symmetric Waves in Flows Past Bluff Bodies

Bhaskar Kumar<sup>1</sup> and Sanjay Mittal<sup>1,2</sup>

**Abstract:** The steady flow past a circular cylinder is investigated. Symmetry conditions are imposed along the centerline of the flow field. The variation of the structure of the recirculation zone with the Reynolds number is studied. The effect of the location of lateral boundary on the flow is analyzed and compared with results from earlier studies. The eddy length varies linearly with  $Re$ . Three kinds of solutions, based on eddy structure, are found for different location of the lateral boundary. Global linear stability analysis has been carried out in a translating frame to determine the convective modes for flow past a circular cylinder. It is found that, compared to the unrestricted flow, the symmetry conditions lead to a significant delay in the onset of convective instability. Detailed results are presented for the  $Re = 500$  flow when the lateral walls are located relatively far off (50 radius) from the cylinder. This situation is expected to be close to unbounded flow past a cylinder. The convectively unstable modes are found to be one of the three kinds. The ones traveling at very low streamwise speed are associated with large scale structures and relatively low frequency. The modes that travel with relatively larger speed lead to the instability of the shear layer and have higher temporal frequency and small scale spatial structure. Instabilities which travel at even higher speeds resemble a swirling flow structure. The results from the linear stability analysis are confirmed by carrying out direct time integration of the linearized disturbance equations. The disturbance field shows transient growth and grows by several orders of magnitude confirming that such flows act as amplifiers. The critical  $Re$  for the onset of convective instability is discussed in the context of earlier results from local analysis.

**Keywords:** Hopf Bifurcation, Convective instability, Circular Cylinder, Linear Stability Analysis, Symmetry of Modes, Finite Element Method, Blockage.

---

<sup>1</sup> Department of Aerospace Engineering, Indian Institute of Technology Kanpur, UP 208 016, India

<sup>2</sup> smittal@iitk.ac.in; Phone: +91 512 2597906; Fax: +91 512 2597561

## 1 Introduction

The importance of absolute/convective analysis in hydrodynamic stability has been highlighted by several researchers in the past (Landau and Lifshitz (1959); Briggs (1964); Bers (1983); Huerre and Monkewitz (1985); Koch (1985); Pierrehumbert (1984)). Typically, convectively unstable flows act as amplifiers (Huerre and Monkewitz (1990)), i.e. they amplify the external inputs which could be environmental disturbances in the experiments or numerical errors in computations. In contrast, absolutely unstable flows act as resonators. Their evolution is dominated by characteristic frequencies of the system. Strictly speaking, these notions are applicable only to parallel flows. Their application to nonparallel flows has been mostly followed via parallel flow approximation valid locally at various stations in the flow field. Further, the adoption of WKBJ and other asymptotic techniques by Chomaz, Huerre, and Redekopp (1988), Monkewitz, Huerre, and Chomaz (1993) and Dizes, Huerre, Chomaz, and Monkewitz (1996) resulted in their extension to weakly nonparallel flows. Recent techniques, developed by Mittal and Kumar (2007), facilitate the investigation of absolute/convective instability of the entire flow field. This method is an extension of the linear stability analysis applicable to nonparallel flows. In this paper we refer to such analysis as global absolute/convective analysis.

Absolute/convective instability of bluff body flows have been investigated by several researchers in the past. Koch (1985) investigated family of symmetric and asymmetric basic wake flows modeled with analytical functions. Huerre and Monkewitz (1985) investigated tangent hyperbolic profiles for inviscid flows. They showed that the flow becomes absolutely unstable when the velocity ratio, defined as the ratio of the difference to the sum of the velocity of the upper and lower streams, becomes larger than 1.315. Convective instability is observed in the range 0.84 to 1.315. Hultgren and Aggarwal (1987) considered a Gaussian velocity profile normalized with the maximum velocity. Though the main focus of their study was modes corresponding to the Karman-type shedding, they also investigated the flow with symmetry conditions enforced at the centerline. In the later case anti-symmetric modes were found to become unstable. Castro (2005) carried out similar computations and studied the effect of the location of lateral boundaries on the critical parameters. A free-slip condition was imposed at the lateral boundaries. It was found that the critical  $Re$  for the convective as well as absolute instability increases when the lateral boundaries are brought closer.

Convectively unstable modes, in some cases, are associated with large transient growth. This may lead a globally absolutely stable flow to show a sustained response, either due to nonlinearity or due to continuous supply of disturbance from external sources. In an interesting study, Fasel and Postl (2006) carried out Direct

Numerical Simulation of a laminar separation bubble formed on a flat plate by introducing a volume force field. It was found that the steady flow profile is highly convectively unstable. In the present work we adopt the method of global analysis to investigate the convective instability for flow past a circular cylinder.

Linear stability analysis of flow past a cylinder reveals the presence of two types of modes: symmetric and anti-symmetric (Zebib (1987)). Various researchers, in the past, have reported the onset of instability for these modes. For example, the absolute instability of the most unstable symmetric mode occurs around  $Re \sim 47$  and leads to von Karman vortex shedding (Zebib (1987); Jackson (1987); Williamson (1989); Norberg (1994); Chen, Pritchard, and Tavener (1995); Ding and Kawahara (1999); Morzynski, Afanasiev, and Thiele (1999); Norberg (2001); Kumar and Mittal (2006a); Kumar and Mittal (2006b)). The instability of anti-symmetric mode occurs at higher  $Re$  and varies significantly with the blockage (Kumar, Kottaram, Singh, and Mittal (2009)). The occurrence of the instability of symmetric modes, in comparison to that of the anti-symmetric modes, at lower  $Re$  has led most of the investigations to be focused on the former ones. However, phenomena like shear/mixing layer instabilities, owe their origin to the instability of anti-symmetric modes. Kumar, Kottaram, Singh, and Mittal (2009) carried out investigation of flow past a cylinder with centerline symmetry. The imposition of centerline suppressed the symmetric modes leaving the anti-symmetric modes unaffected. Both, absolute and convective modes were investigated. Although some results for the low blockage were discussed, their study of convective instability was mostly focused towards high blockage cases. In the present study we examine the anti-symmetric convective modes in flow past a cylinder for low blockage. These are expected to be much closer to results for an unbounded flow.

The paper is arranged in the following sequence. In the Section 2, we present the governing equations. The numerical technique utilized to carry out the computations is same as that used in our earlier studies (Mittal and Kumar (2007); Mittal., Kottaram, and Kumar (2008); Kumar, Kottaram, Singh, and Mittal (2009)). A short description for the same is, however, presented in Section 3. This is followed by the description for problem set-up and boundary conditions in Section 4. The results are presented and discussed in Section 5. We end with conclusions in Section 6.

## 2 The Governing Equations

### 2.1 The incompressible flow equations

Let  $\Omega \subset R^{n_{sd}}$  and  $(0, T)$  be the spatial and temporal domains respectively, where  $n_{sd}$  is the number of space dimensions, and let  $\Gamma$  denote the boundary of  $\Omega$ . The spatial and temporal coordinates are denoted by  $\mathbf{x}$  and  $t$ . The Navier-Stokes equations

governing incompressible fluid flow are

$$\rho \left( \frac{\partial \mathbf{u}}{\partial t} + \mathbf{u} \cdot \nabla \mathbf{u} \right) - \nabla \cdot \boldsymbol{\sigma} = \mathbf{0} \quad \text{on } \Omega \times (0, T), \quad (1)$$

$$\nabla \cdot \mathbf{u} = 0 \quad \text{on } \Omega \times (0, T). \quad (2)$$

Here  $\rho$ ,  $\mathbf{u}$  and  $\boldsymbol{\sigma}$  are the density, velocity and the stress tensor, respectively. The stress tensor is written as the sum of its isotropic and deviatoric parts:

$$\boldsymbol{\sigma} = -p\mathbf{I} + \mathbf{T}, \quad \mathbf{T} = 2\mu\boldsymbol{\varepsilon}(\mathbf{u}), \quad \boldsymbol{\varepsilon}(\mathbf{u}) = \frac{1}{2}((\nabla \mathbf{u}) + (\nabla \mathbf{u})^T), \quad (3)$$

where  $p$  and  $\mu$  are the pressure and coefficient of dynamic viscosity, respectively. The above set of equations can be solved along with suitable initial and boundary conditions to obtain the time evolution of the flow field. The steady state solution can be computed by simply dropping the time derivative term from Equation (1).

## 2.2 Equations for the perturbation

We decompose the unsteady solution as a combination of the steady state solution and perturbation.

$$\mathbf{u} = \mathbf{U} + \mathbf{u}', \quad p = P + p'. \quad (4)$$

Here,  $\mathbf{U}$  and  $P$  represent the steady state solution while  $\mathbf{u}'$  and  $p'$  are the perturbation fields of the velocity and pressure, respectively. Substituting Eq. (4) in Eqs. (1)-(2) and subtracting from them the equations for steady flow one obtains:

$$\rho \left( \frac{\partial \mathbf{u}'}{\partial t} + \mathbf{u}' \cdot \nabla \mathbf{U} + \mathbf{U} \cdot \nabla \mathbf{u}' + \mathbf{u}' \cdot \nabla \mathbf{u}' \right) - \nabla \cdot \boldsymbol{\sigma}' = \mathbf{0} \quad \text{on } \Omega \times (0, T), \quad (5)$$

$$\nabla \cdot \mathbf{u}' = 0 \quad \text{on } \Omega \times (0, T). \quad (6)$$

Here,  $\boldsymbol{\sigma}'$  is the stress tensor for the perturbed solution computed using Eq. (3).

## 2.3 Linearized equations for the perturbation

Assuming that the perturbation field is small, the nonlinear term from Eq. (5) is dropped to obtain the linearized momentum equation for the perturbation. The continuity equation remains as it is. The linearized disturbance equations are:

$$\rho \left( \frac{\partial \mathbf{u}'}{\partial t} + \mathbf{u}' \cdot \nabla \mathbf{U} + \mathbf{U} \cdot \nabla \mathbf{u}' \right) - \nabla \cdot \boldsymbol{\sigma}' = \mathbf{0} \quad \text{on } \Omega \times (0, T), \quad (7)$$

$$\nabla \cdot \mathbf{u}' = 0 \quad \text{on } \Omega \times (0, T). \quad (8)$$

## 2.4 Equations for the linear stability analysis

To carry out the global linear stability analysis we write the perturbation equations in a frame moving with a velocity  $\mathbf{c}$  with respect to the laboratory frame. This modification allows us to investigate both the absolute as well as convective instability in the same setting (Mittal and Kumar (2007)). The change of frame is effected by the following transformations:

$$\mathbf{x} = \mathbf{z} + \mathbf{c}t, \quad \nabla_{\mathbf{x}} = \nabla_{\mathbf{z}}, \quad \left. \frac{\partial}{\partial t} \right|_{\mathbf{x}} = \left. \frac{\partial}{\partial t} \right|_{\mathbf{z}} - \mathbf{c} \cdot \nabla_{\mathbf{z}}. \quad (9)$$

Here,  $\mathbf{x}$  and  $\mathbf{z}$ , respectively, denote the position vectors of a point in the flow field, with respect to the laboratory frame and the translating frame. We further assume that the disturbances are of the following form:

$$\mathbf{u}'(\mathbf{x}, t) = \hat{\mathbf{u}}(\mathbf{x} - \mathbf{c}t)e^{\lambda t}, \quad (10)$$

$$p'(\mathbf{x}, t) = \hat{p}(\mathbf{x} - \mathbf{c}t)e^{\lambda t}. \quad (11)$$

Substituting Eqs. (10)-(11) in Eqs. (7)-(8) we get:

$$\rho(\lambda \hat{\mathbf{u}} + \hat{\mathbf{u}} \cdot \nabla_{\mathbf{z}} \mathbf{U} + (\mathbf{U} - \mathbf{c}) \cdot \nabla_{\mathbf{z}} \hat{\mathbf{u}}) - \nabla_{\mathbf{z}} \cdot \hat{\boldsymbol{\sigma}} = \mathbf{0} \quad \text{on } \Omega \quad (12)$$

$$\nabla_{\mathbf{z}} \cdot \hat{\mathbf{u}} = 0 \quad \text{on } \Omega. \quad (13)$$

It is important to note that the base flow,  $\mathbf{U}(\mathbf{x})$ , is computed in the laboratory frame. However, in Eqs. (12)-(13), it is to be interpreted as  $\mathbf{U}(\mathbf{z} + \mathbf{c}t)$ . Therefore, in the moving frame, the base flow varies with time. At  $t = 0$ ,  $\mathbf{z} = \mathbf{x}$  and one can use the same base flow as computed in the stationary frame. Thus, this analysis, for determining the global convective instability, is valid in an instantaneous sense.

## 3 Numerical Technique

In order to solve the above mentioned initial boundary value problems we utilize the stabilized finite element formulation as presented in Tezduyar, Mittal, Ray, and Shih (1992). The SUPG (Streamline-Upwind/Petrov-Galerkin) and PSPG (Pressure-Stabilizing/Petrov-Galerkin) stabilization technique (Tezduyar, Mittal, Ray, and Shih (1992)) is employed to stabilize the computations against spurious numerical oscillations. The SUPG formulation for convection dominated flows was introduced by Hughes and Brooks (1979) and Brooks and Hughes (1982). The Petrov-Galerkin term for Stokes flows, to admit the use of equal-order interpolations for velocity and pressure without producing oscillations in the pressure field, was proposed by Hughes, Franca, and Balestra (1986). Tezduyar, Mittal, Ray, and Shih

(1992) proposed a formulation using the SUPG and PSPG stabilization for finite Reynolds number flows.

Since the formulation used here is same as that presented in our earlier works (Mittal and Kumar (2007); Mittal, Kottaram, and Kumar (2008); Kumar, Kottaram, Singh, and Mittal (2009)) one may refer these to see the explicit form of the equations. Further, it may be noted that for unsteady computations, the algebraic equation systems resulting from the finite-element discretization of the flow equations are solved using the Generalized Minimal RESidual (*GMRES*) technique (Saad and Schultz (1986)) in conjunction with diagonal preconditioners. For carrying out the linear stability analysis, first, the steady-state solutions at various  $Re$  are obtained by solving the governing equations without the unsteady terms and progressively increasing the  $Re$ . The linear stability analysis, of these steady states, involves the solution to an eigenvalue problem. A sub-space iteration procedure (Morzynski, Afanasiev, and Thiele (1999)) in conjunction with shift-invert transformation is utilized. Double precision arithmetic is used in all the computations.

It may pointed out that the above mentioned approach, based on the finite element method, has been successfully applied to solving various fluid flow problems in the past. A good quality mesh is a pre-requisite to obtaining good quality solutions. The generation of mesh for complex geometries, especially in 3D, can be a very cumbersome process. Recently, a number of meshless methods have been developed that may help one to get around the process of generating a mesh. Examples of such approaches are the element free Galerkin method (Belytschko, Organ, and Y.Krongauz (1994)), reproducing kernel particle method (Liu, Chen, Chang, and Belytschko (1996)), meshless local boundary equation (MLBIE) method (Zhu, Zhang, and Atluri (1998)) and meshless local Petrov-Galerkin method (MLPG) (Atluri and Zhu (1998, 2000); Atluri and Shen (2002); Atluri, Han, and Rajendran (2003)). Atluri and Zhu (2000) state that the main objective of meshless methods is to get rid of or at least alleviate the difficulty of meshing and remeshing the entire structure, by only adding or deleting nodes in the entire structure. Lin and Atluri (Lin and Atluri (2002)) compared the SUPG and MLPG approaches and for convection diffusion problems and found them to provide comparable results. Recently, Mohammadi (2008) extended the MLPG method for computation of steady incompressible flows, governed by the Navier-Stokes equations, in the vorticity-stream function formulation. He introduced a new upwinding scheme to stabilize the convection operator in the streamline direction.

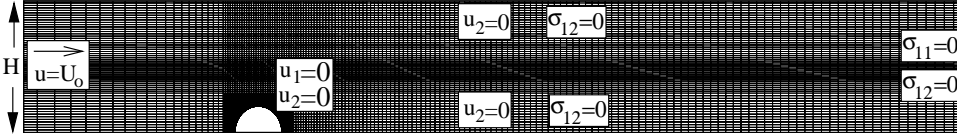


Figure 1: Close-up view of a typical finite element mesh. The conditions on the respective boundaries are also shown.

## 4 Problem set-up

### 4.1 Finite element mesh and the boundary conditions

A typical finite element mesh is shown in the Figure 1. Four noded quadrilateral elements with equal order interpolation for velocity and pressure are employed. Sufficient grid points are used close to the cylinder to resolve the boundary layer and separating shear layer. To capture the modes that are symmetric with respect to the wake centerline only one half of the cylinder is considered. The lateral boundary is located at a distance  $H$  from the center of the cylinder. Computations are carried out for various values of  $H$ . The upstream and downstream boundaries are located at  $50D$  and  $150D$ , respectively, from the center of the cylinder. Free-stream value is assigned to the velocity at the upstream boundary. At the downstream boundary, a Neumann-type boundary condition for the velocity is specified that corresponds to zero stress vector. On the upper and lower boundaries a "slip-wall" boundary condition is employed, i.e., the component of velocity normal to and the component of stress vector along these boundaries are prescribed a zero value. For the linear stability analysis, the boundary conditions are the homogeneous versions of the ones used for determining the steady state solutions.

### 4.2 The nondimensional parameters

The radius of the cylinder,  $R$ , is used for nondimensionalizing the length scales while the free stream speed,  $U$ , is used as the characteristic speed. Time is nondimensionalized with  $R/U$ . The Reynolds number,  $Re$ , is defined as  $UD/\nu$ ,  $\nu$  being the kinematic viscosity of the fluid and  $D$ , the diameter. The cross-stream width of the domain,  $H$ , is expressed in terms of  $R$ . For the linear stability analysis, each component of the frame velocity,  $\mathbf{c}$ , is nondimensionalized with  $U$ . Another parameter that is referred to is the Strouhal number,  $St$ . It is defined as  $fD/U$ , where  $f$  is the frequency of signal of interest. The drag and lift coefficients per unit length are represented by  $C_D$  and  $C_L$ , respectively. They are computed by performing an integration, that involves the pressure and viscous stresses, around the circumference

of the cylinder and non-dimensionalized with respect to the dynamic pressure and diameter of the cylinder.

## 5 Results

### 5.1 Steady flow

The time dependent terms in Equations (1) and (2) are dropped to compute the steady flow past a half cylinder. We note that the steady flow past a circular cylinder is symmetric about the wake centerline. Hence the flow being computed here represents the steady flow past a full cylinder. In the past, this flow has been motivated to represent the flow past a cascade of circular cylinders.

Typically, the investigations of steady flow past a cylinder have focused on monitoring the length and width of the wake bubble, maximum vorticity on the surface of the cylinder and the drag coefficient. It is found both from the theoretical results as well as from computations (Smith (1979); Fornberg (1985); Fornberg (1991); Gajjar and Azzam (2004)), that the bubble length increases linearly with  $Re$ . Smith (1979) suggested that the width of the wake bubble grows as  $O(Re^{1/2})$ . Fornberg (1985) showed that it grows as  $O(Re^{1/2})$  up to  $Re = 300$  and increases linearly thereafter. It was later shown (Fornberg (1991)) that for an unbounded flow, both, length and width of the bubble grow linearly with  $Re$ . Gajjar and Azzam (2004) showed that, although it grows for low  $Re$ , for high enough  $Re$  the width of the bubble is limited by the blockage and gets saturated.

Table 1: Bubble length at various  $Re$  from different studies. The abbreviations used are: P: Present results; F: Results from Fornberg (1991); G: Results from Gajjar and Azzam (2004).

$H$	Researcher	100	400	500	600	800	1000	1500	2000	2500
5	P	10.97	37.59	46.31	55.01	72.42	89.83	133.43	177.16	221.09
	F	10.3	35.3	43.5	51.7	68.1				
10	P	11.92	41.72	51.45	61.10	80.12	99.02	145.47	191.52	
	G	11.92	41.7	51.43	61.1	80.2	98.97	145.4	191.6	
	F	11.9	41.5	51.1	60.6	79.3				
50	P	13.28	56.44	73.13						
	G	13.28	56.6	73.74						
	F	13.2	56.1	72.8						

Tables 1–4 show a comparison of the characteristic parameters obtained from the present computations with those reported earlier. It can be seen that the present results are in very good agreement with those reported by Gajjar and Azzam (2004)Gaj-

Table 2: Bubble width at various  $Re$  from different studies. The abbreviations used are: P: Present results; F: Results from Fornberg (1991); G: Results from Gajjar and Azzam (2004).

$H$	Researcher	100	400	500	600	800	1000	1500	2000	2500
5	P	2.52	3.28	3.34	3.39	3.44	3.47	3.52	3.55	3.57
	F	2.37	2.87	2.92	2.95	2.99				
10	P	2.69	3.97	4.08	4.23	4.73	5.21	6.24	6.98	
	G	2.69	3.96	4.08	4.24	4.75	5.23	6.26	6.98	
	F	2.71	3.98	4.10	4.26	4.75				
50	P	2.80	9.29	17.62						
	G	2.87	9.39	17.75						
	F	2.88	9.02	16.4						

Table 3: Drag coefficient at various  $Re$  from different studies. The abbreviations used are: P: Present results; F: Results from Fornberg (1991); G: Results from Gajjar and Azzam (2004).

$H$	Researcher	100	400	500	600	800	1000	1500	2000	2500
5	P	1.41	1.07	1.04	1.02	0.99	0.98	0.96	0.95	0.95
	F	1.61	1.22	1.18	1.16	1.12				
10	P	1.25	0.92	0.89	0.88	0.86	0.85	0.83	0.82	
	G	1.26	0.92	0.90	0.88	0.86	0.85	0.83	0.82	
	F	1.25	0.91	0.88	0.86	0.83				
50	P	1.08	0.67	0.57						
	G	1.08	0.66	0.57						
	F	1.072	0.672	0.581						

jar and Azzam (2004). All the results presented here have been checked for grid independence. For example, the difference between the bubble lengths computed for  $H = 10$  case, at  $Re = 1000$ , with two different finite element meshes consisting of 57,313 and 86,419 nodes, is less than 0.1%. As reported by Gajjar and Azzam (2004) the computations for  $H = 50$  and beyond are very demanding on computational resources. With our computational resources we were unable to compute flows for  $Re > 500$  accurately for  $H = 50$ . Figure 2 shows the variation of bubble length and width with  $Re$  for various domain width. Good agreement with data from Gajjar and Azzam (2004) is apparent from this figure. The linear growth of bubble length with  $Re$  can be clearly observed. The variation of  $C_D$  and maximum vorticity on the cylinder surface ( $\zeta_m$ ) with  $Re$  is shown in the Figure 3. Very good

Table 4: Maximum vorticity on the cylinder surface at various  $Re$ , from different studies. The abbreviations used are: P: Present results; F: Results from Fornberg (1991); G: Results from Gajjar and Azzam (2004).

$H$	Researcher	100	400	500	600	800	1000	1500	2000	2500
5	P	11.18	22.74	25.52	28.04	32.51	36.45	44.84	51.92	58.16
	F	12.2	24.7	27.7	30.4	35.1				
10	P	10.26	20.74	23.28	25.58	29.67	33.27	40.93	47.39	
	G	10.28	20.76	23.30	25.62	29.72	33.35	41.06	47.55	
	F	10.3	20.6	23.1	25.3	29.3				
50	P	9.13	16.66	17.06						
	G	9.16	16.64	17.06						
	F	9.2	16.7	17.4						

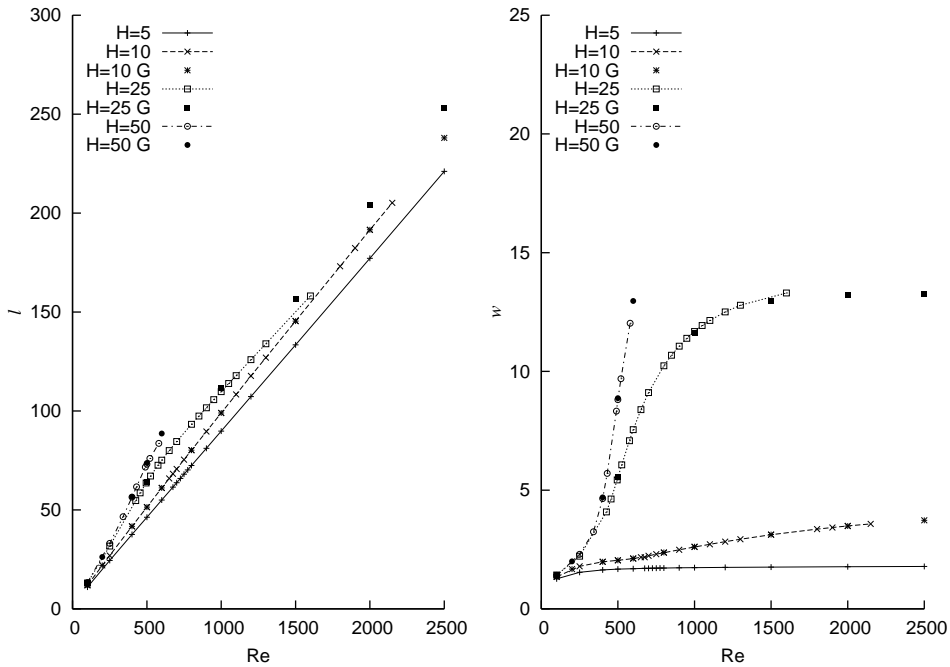


Figure 2: Variation of the bubble length ( $l$ ) and width ( $w$ ) with  $Re$ . In the figure  $G$  refers to results from Gajjar and Azzam (2004).

agreement with the results from Gajjar and Azzam (2004) is observed.

The streamline and vorticity contours for  $H = 5, 10$  and  $50$  are shown in Figures 4, 5

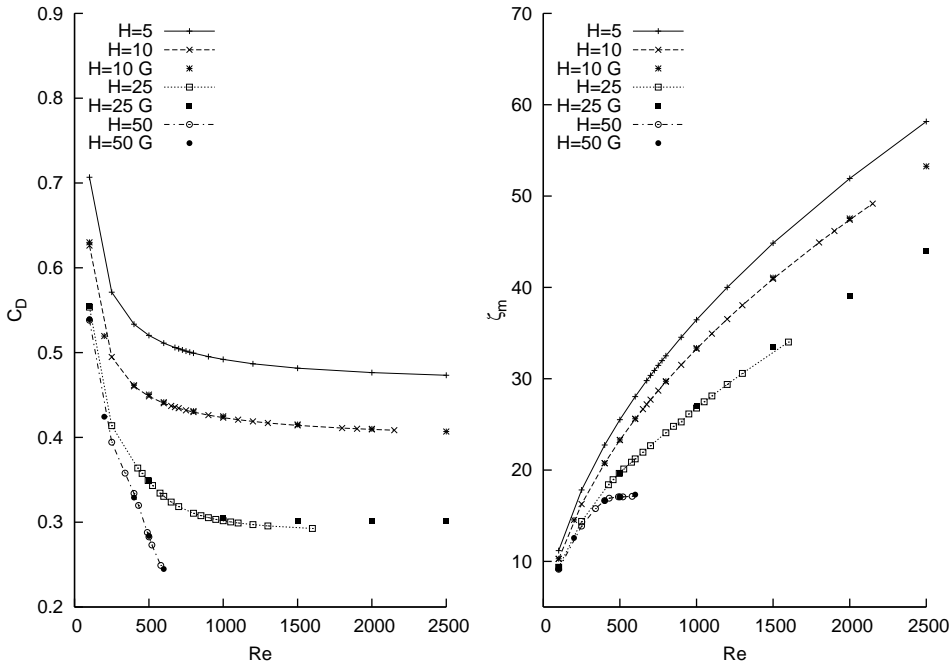


Figure 3: Variation of the drag coefficient ( $C_D$ ) and the maximum vorticity on the cylinder surface ( $\zeta_m$ ) with  $Re$ . In the figure  $G$  refers to results from Gajjar and Azzam (2004).

and 6, respectively. To highlight the flow features the cross flow dimension is stretched. With respect to the blockage the flow can be broadly classified in three categories.  $H = 5$  flow, shown in Figure 4, is typical of very high blockage. When the adjacent boundaries are extremely close to the cylinder the recirculation bubble is slender. The length of the bubble increases with  $Re$ . Following the nomenclature proposed by Gajjar and Azzam (2004) we refer to these as 'Type I' solutions. As the lateral walls are shifted away from the cylinder the solution changes to 'Type II'. Figure 5 shows an example of the Type II flow, for  $H = 10$ . The flow begins to develop features, associated with low blockage, close to the reattachment point. An unusual increase in the bubble width near the downstream end of the bubble is observed. This feature of the bubble is similar to that observed in the Sadovskii type of vortex (Sadovskii (1971)) and was also reported by Gajjar and Azzam (2004). The bubble length increases linearly with  $Re$ . However, the bubble width saturates for large  $Re$ . Type III solution is observed for even lower blockage cases. Figure 6

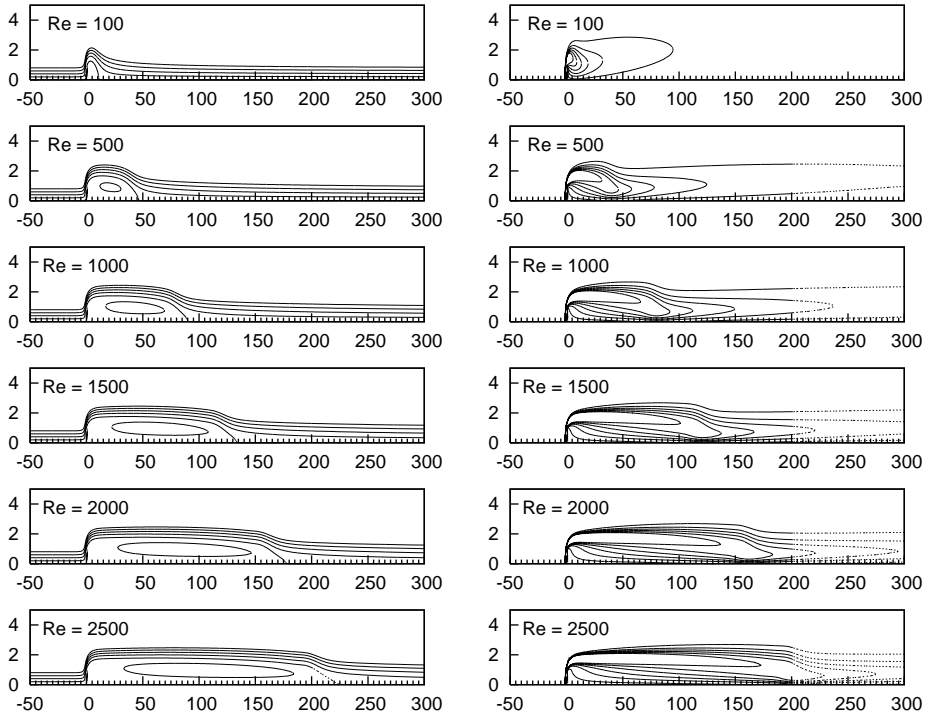


Figure 4:  $H = 5$  steady flow past a circular cylinder: stream function (left) and vorticity contours (right) at various values of  $Re$ . Solid lines indicate positive while the broken ones indicate negative values.

shows the solution for  $H = 50$  at various  $Re$ . Both, the length as well as width of the bubble become very large. A large Sadvskii vortex (Sadvskii (1971)) is observed in the wake of the cylinder. While the length of the bubble increases linearly with  $Re$ , the bubble width is constrained by the lateral wall and, therefore, is expected to level out for large  $Re$ .

## 5.2 Linear stability analysis in a moving frame

In order to carry out linear stability analysis the eigenvalue problem represented by the equations (12) and (13) is solved with the homogeneous boundary conditions. Detailed results are presented for  $H = 50$ . This leads to very small blockage and is expected to represent the unbounded flow past a circular cylinder. The mesh being utilized has sufficient resolution to lead to mesh-independent results. One

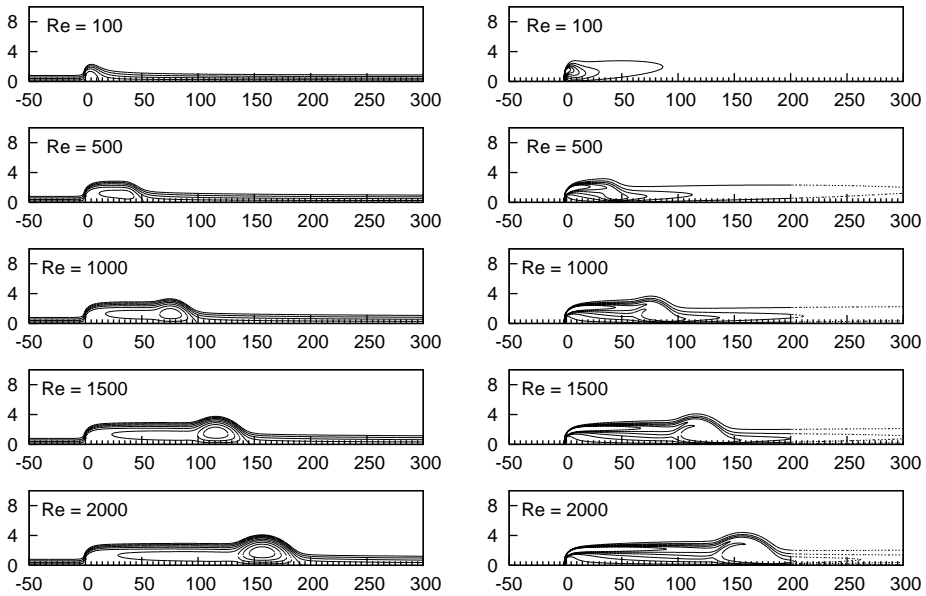


Figure 5:  $H = 10$  steady flow past a circular cylinder: stream function (left) and vorticity contours (right) at various values of  $Re$ . Solid lines indicate positive while the broken ones indicate negative values.

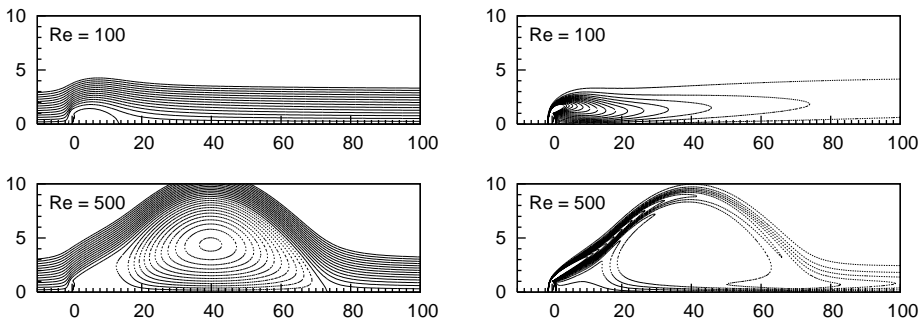


Figure 6:  $H = 50$  steady flow past a circular cylinder: stream function (left) and vorticity contours (right) at various values of  $Re$ . Solid lines indicate positive while the broken ones indicate negative values.

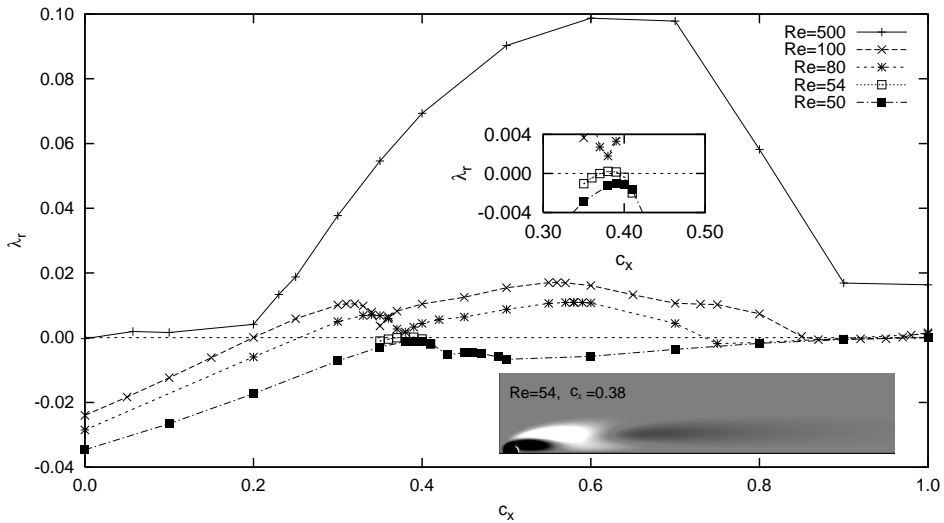


Figure 7: Variation of the growth rate of the most unstable eigenmode with  $c_x$  for different  $Re$ . The vorticity field of the unstable eigenmode close to the onset of the instability ( $Re = 54$ ,  $c_x = 0.38$ ) is also shown.

such study, for  $H = 10$ , was presented in an earlier work (Kumar, Kottaram, Singh, and Mittal (2009)) In the present work we track the disturbances which move in the streamwise direction, i.e.,  $c_y$  is prescribed a zero value. Figure 7 shows the variation of growth rate  $\lambda_r$  with  $c_x$ , at different  $Re$ . This figure shows the data for the rightmost eigenvalue, i.e., the one that has the largest real part. It is seen that the growth rate, in general, increases with increase in  $Re$ . The variation of  $\lambda_r$  with  $c_x$ , for each  $Re$  is interesting. For relatively large  $Re$ ,  $\lambda_r$  first increases and then decreases as  $c_x$  increases. The critical  $Re$  for the onset of convective instability is  $Re = 54$ . Also shown in the same figure is the unstable mode obtained a little beyond the onset. For a full cylinder the onset of convective instability, from global analysis, occurs at  $Re = 4$  (Mittal and Kumar (2007)). We, therefore, conclude that the imposition of symmetry at the wake centerline leads to a delay in the onset of convective instability. Figure 8 shows the variation of the Strouhal number ( $St$ ) with  $c_x$  for various  $Re$ . It can be seen that for each  $Re$  there is a range of  $c_x$  for which  $St$  is nonzero. Over all, the  $St$  is found to increase with  $Re$ . This trend, however, is not strictly valid for all values of  $c_x$ . This figure brings out the richness in this flow regarding the various eigenmodes associated with it. It shows how the different modes compete to show their dominance at various  $c_x$  and  $Re$ .

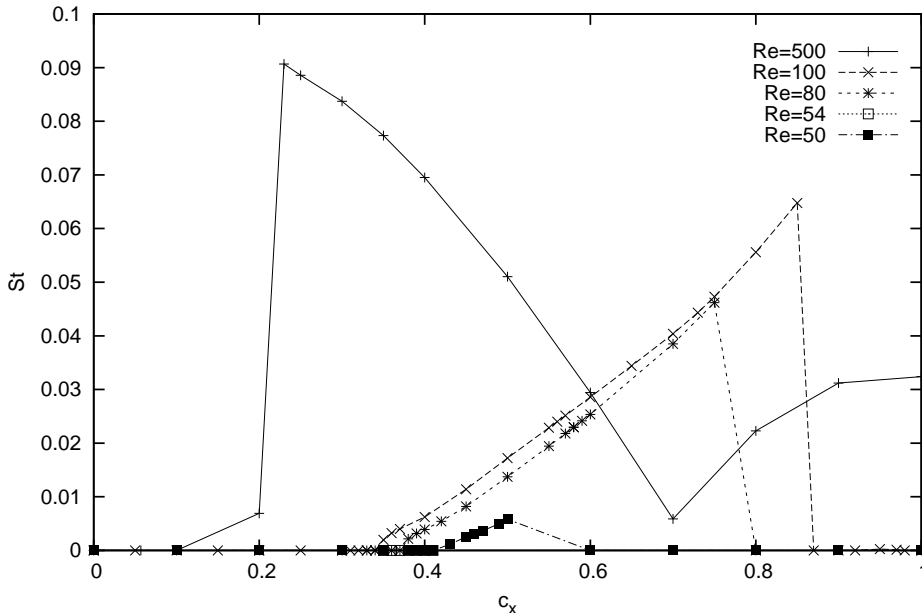


Figure 8: Variation of the Strouhal number of the most unstable eigenmode with  $c_x$  for different  $Re$

### 5.2.1 Most unstable modes for $Re = 500$

From Figure 7 it is seen that, for  $Re = 500$ , the growth rate increases quite rapidly with  $c_x$ . At  $c_x = 0$  the growth rate is slightly negative. This reflects the marginal absolute stability of the flow. The flow is found to be unstable beyond  $c_x \sim .057$ . This marks the onset of convective instability of the flow. For this mode the  $St$  is found to be zero. Figure 9 shows the real part of the most unstable modes obtained for different values of  $c_x$ . The modes can be classified into three types. The first type of modes are the ones which have bubble like structure in the wake. These are found for  $0.0 \leq c_x \leq 0.2$ . The second type of modes have small scale structures in the shear layer emanating from the cylinder. These are observed for  $0.23 \leq c_x \leq 0.7$  and are very typical of the shear layer vortices that have been reported in experiments at larger  $Re$ . The third type of modes, shown for  $c_x = 1.0$ , resemble a tornado. These modes have very low growth rate. However, if excited sufficiently, they can possibly lead to tornado type of motion. It is possible that for very high  $Re$  they may show large growth rate.

An important point which may be noted from Figure 8 is that, for  $Re = 500$ , there

is a sudden increase in the value of  $St$  at  $c_x \sim 0.23$ . This is corroborated with the appearance of small scale shear layer vortices in the eigenmodes (cf. figure 9). Further, Figure 7 shows that there is a change in the slope of the growth rate curve at  $c_x = 0.2$ . This is an instance of mode switch where the high frequency shear layer mode takes over the low frequency mode.

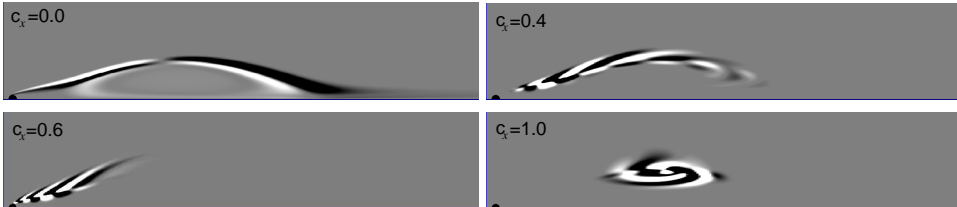


Figure 9: Vorticity field of the real part of the most unstable mode for  $Re = 500$  at different values of  $c_x$ .

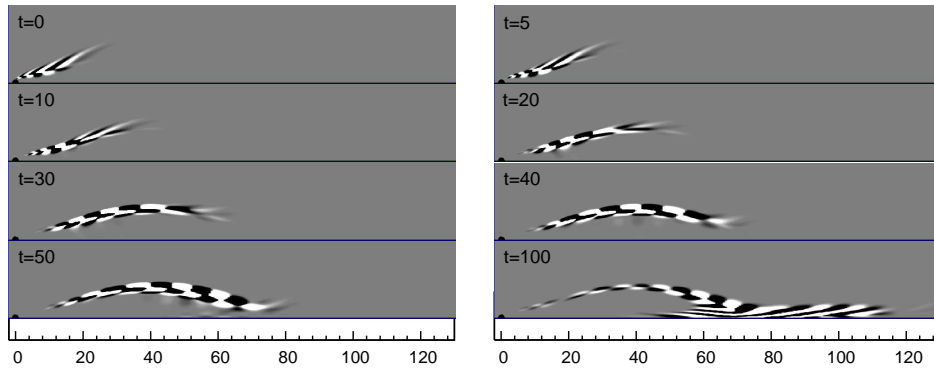


Figure 10: Snap shots of the disturbance vorticity field at different time instants computed from the linearized disturbance equation. The initial disturbance field is the most unstable mode for  $Re = 500$  and  $c_x = 0.6$ .

### 5.3 Direct time integration of disturbance equations for $Re = 500$ flow

#### 5.3.1 Linearized disturbance equations

Direct time integration of the linearized disturbance equations (7) and (8) is carried out to confirm the results from the linear stability analysis. The kinetic energy of

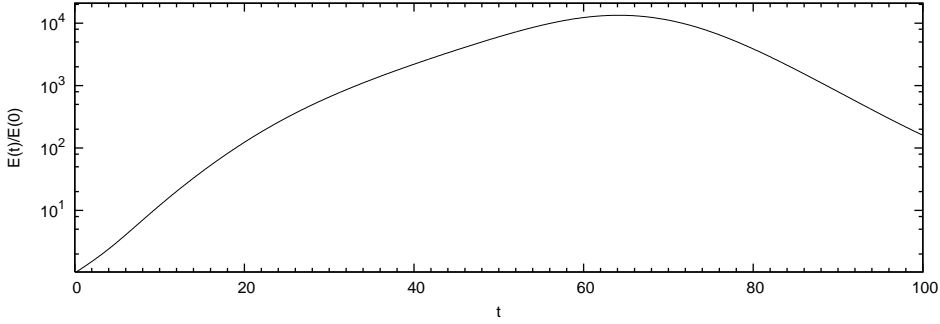


Figure 11: Variation of the normalized disturbance energy ( $E(t)/E(0)$ ) of the flow field (please see the caption of Figure 10 for details).

the disturbance field in the flow domain,  $\Omega$ , is defined as:

$$E(t) = \frac{\rho}{2} \int_{\Omega} \mathbf{u}' \cdot \mathbf{u}' d\Omega . \quad (14)$$

We consider the case when an eigenmode, as defined by Equations (10) and (11), is used as an initial condition for the computations. In this situation the kinetic energy can be expressed as:

$$E(t) = \frac{\rho}{2} e^{2\lambda_r t} \int_{\Omega} \hat{\mathbf{u}} \cdot \bar{\hat{\mathbf{u}}} d\Omega . \quad (15)$$

Here, the overbar indicates the complex conjugate while  $\lambda_r$  is the growth rate of the mode. This leads to the following expression for an estimate of  $\lambda_r$ .

$$\lambda_r = \frac{1}{2t} \ln \frac{E(t)}{E(0)} . \quad (16)$$

The computations begin with the mode corresponding to the most unstable convective mode, i.e. the mode for  $c_x = 0.6$ . Figure 10 shows the vorticity of the disturbance field at various time instants of the simulation. The development of the shear layer vortices is observed very clearly in this figure. The corresponding evolution of the disturbance kinetic energy is shown in the Figure 11. It can be seen that the energy grows upto 10,000 times the initial energy of the disturbance in a period of about 60 time units. This reflects an almost explosive growth of the shear layer instability. After a certain time the kinetic energy of the disturbance starts to decay. This is expected of a convective instability in a finite domain. Using the value of energy at  $t = 5$  and the expression given by Equation (16) the growth

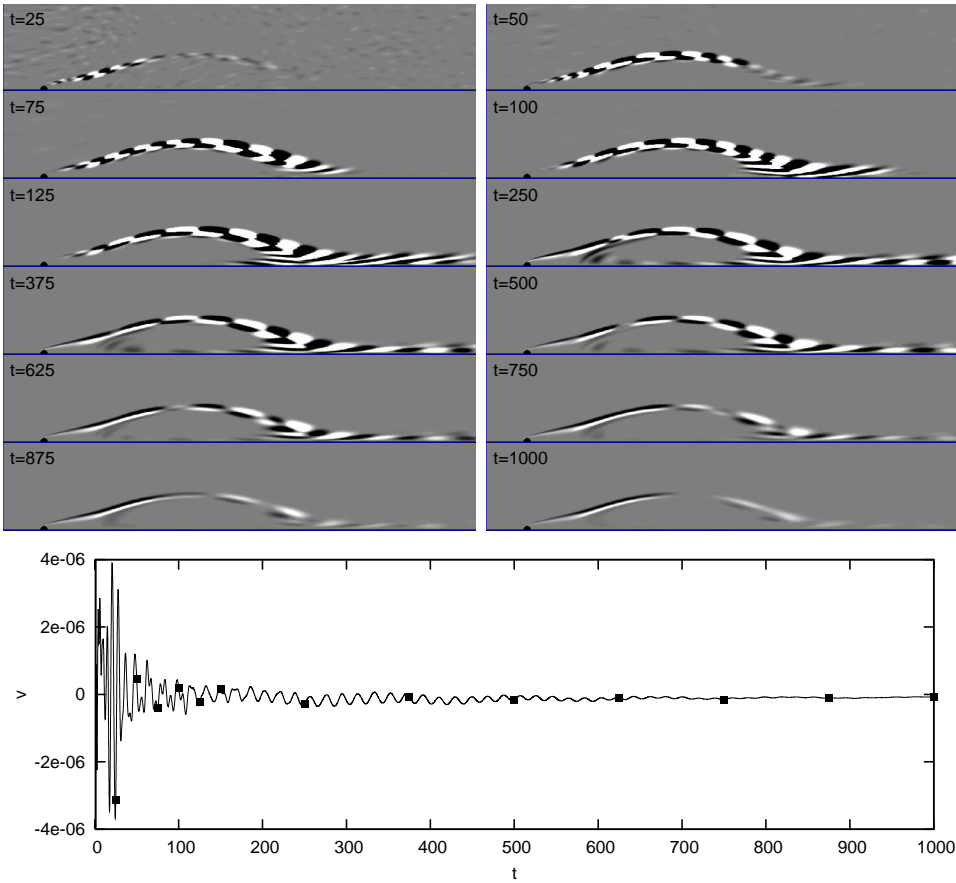


Figure 12: Time evolution of the vorticity of the computed disturbance field obtained from the time integration of the nonlinear disturbance equations. The initial condition is a randomized disturbance field having amplitude of the order of  $5.0 \times 10^{-5}$ . The line plot in the last row shows the time history of the cross-stream component of the velocity recorded at  $(1.0R, 1.0R)$  from the center of the cylinder. The square dots indicate the time instants at which the flow pictures are shown.

rate is found to be  $\lambda_r \sim 0.099$ . This value is in good agreement with that from the linear stability analysis which predicts  $\lambda_r \sim 0.0987$ . The convective speed of the disturbance from this figure is also estimated to be close to 0.6 for  $t$  near 0. The good agreement in the results from the linear stability analysis and the direct time integration of the linearized disturbance equations adds to our confidence in the present analysis. At this point we note that, since the modes under consideration

are convectively unstable, the energy estimate given by Equation (16) is valid only in the frame traveling with the mode. However, for small  $t$  it is expected that the mode will retain its form and growth rate as it moves in the laboratory frame.

Similar kinds of rapidly growing disturbances have been reported earlier in other situations. For example, Fasel and Postl (2006) showed that the steady state separation bubble of the boundary layer over a flat plate is associated with large convective growth. This leads to growth of perturbations by several orders of magnitude. As a result extremely small environmental disturbances can grow and lead to instabilities which are not intrinsic to the flow. A similar situation can arise in numerical computations of flows that are marginally absolutely stable but highly unstable with respect to convective disturbances. Despite the flow being absolutely stable, this can lead to sustained instabilities because of very large growth of round off errors.

### 5.3.2 Non-linear disturbance equations

In order to examine the effect of nonlinearity on the growth of the disturbance we carry out computations with non-linear disturbance equations. The steady flow is perturbed by a random velocity field having amplitude of the order of  $5.0 \times 10^{-5}$ . Unlike the linearized disturbance equations, the nonlinear equations limit the growth of disturbance amplitude. Figure 12 shows the results from the direct time integration of the non-linear disturbance equations. It is observed that the disturbances which resemble the shear layer modes predicted by the global linear stability analysis, develop with time. After an initial growth they start decaying. At  $t \sim 1000$  the disturbance resembles the modes which are predicted by the stability analysis for low values of  $c_x$  (Figure 9). These modes have long streaks of vorticity along the shear layer. The simulation testifies to the fact that the modes which have larger growth rate dominate the flow and those which have larger speeds leave the flow field earlier. The last row of Figure 12 shows the time history of the cross-stream component of the velocity recorded at a point located at  $(1.0R, 1.0R)$  from the center of the cylinder. This point is located close to the shear layer separating from the cylinder. After initial transience, oscillations due to the shear layer vortices are observed. They ride on a very low frequency wave that are due to the excitation of the modes traveling at relatively lower speeds.

## 5.4 Local versus global analysis

In the past, local analysis has been carried out for various cases of shear flows. The mixing layer profile modeled by the hyperbolic tangent function was studied by Huerre and Monkewitz (1985). They concluded that an inviscid flow with such a profile would become convectively unstable if the velocity ratio, a suitable measure of the reverse flow, exceeds 0.84. It becomes absolutely unstable for velocity ratio

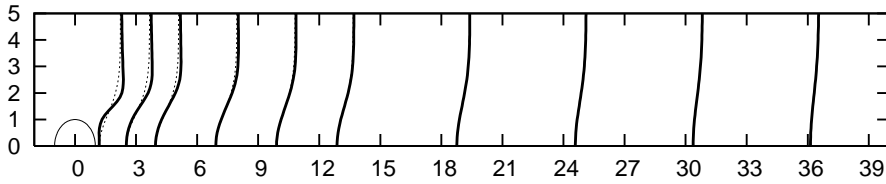


Figure 13: Steady flow past a half cylinder: velocity profiles at various stream wise locations shown in solid lines. Also shown in broken lines are the profiles assuming a Gaussian distribution given by Equation (18). The figure corresponds to  $H = 50$  and  $Re = 54$ .

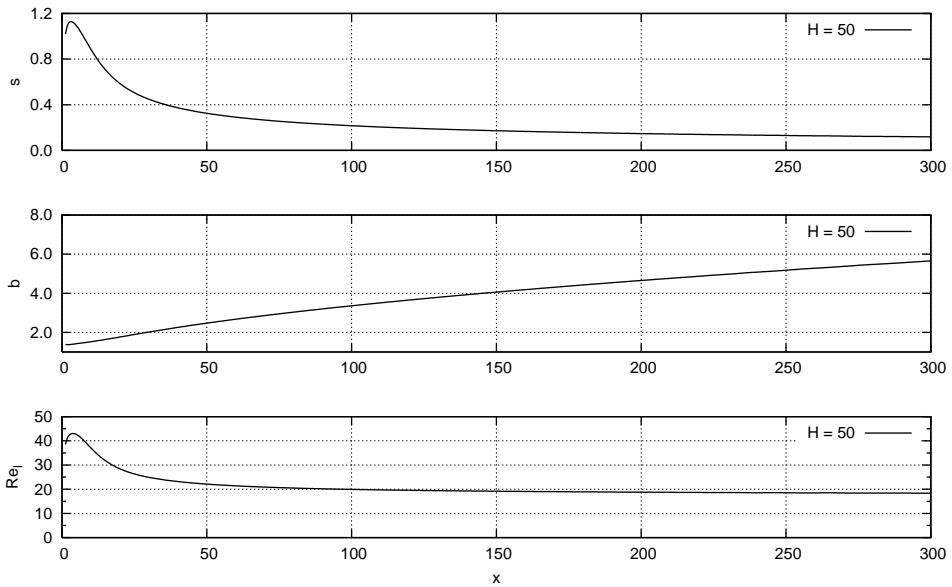


Figure 14:  $H = 50$  steady flow past a half cylinder: stream wise variation of the effective value of  $s(x) = (u(x, y = H) - u(x, y = 0)) / u(x, y = H)$ , half wake width and the local Reynolds number,  $Re_l$ , based on  $s(x) u(x, y = H)$  and  $b$ .

greater than 1.315. Another case, studied by Hultgren and Aggarwal (1987), is that of a Gaussian profile given by the following equation:

$$u = 1 - s e^{-y^2 \ln(2)}. \tag{17}$$

Here, the speed is normalized by its maximum value,  $y$  by the wake half-width and  $s$  is a measure of the reverse flow. Hultgren and Aggarwal (1987) considered unbounded/free viscous shear layers. From their analysis, they concluded that the Karman type mode becomes convectively unstable at  $Re = 3.76$  while the modes obtained with symmetry condition enforced at the wake centerline loose stability at  $Re = 53$ . The  $Re$ , in their work, is based on the maximum speed difference and wake half-width. With this definition the critical  $Re$  is found to be independent of the amount of reverse flow. A similar study with the Gaussian profile (Eq. 17) was carried out by Castro (2005). In addition to the symmetry condition imposed at the centerline, Castro (2005), in his investigation, considered the flow bounded by slip walls placed at finite distance. The distance between the wake centerline and the side walls, represented by  $H$ , was varied. It was found that the critical  $Re$  for  $H = 100, 10, 5$  and  $3$  is  $52.99, 53.06, 57.30$  and  $97.11$ , respectively.

We compare our results from the global stability analysis of the non parallel flow with those of earlier researchers. Recall, the critical  $Re$  for the onset of convective instability, from the global stability analysis is  $54$ . Figure 13 shows the velocity profiles at different stations downstream of the cylinder for the corresponding steady flow along with the Gaussian profile,  $u_G(x, y)$ . The expression for the Gaussian profile is given as follows:

$$u_G(x, y) = u(x, y = H) \left[ 1 - s(x) e^{-\left(\frac{y}{b(x)}\right)^2 \ln(2)} \right], \quad (18)$$

Here,  $s(x)$  is the reverse flow parameter and  $b(x)$  the wake half width. They are calculated from the velocity profiles of the actual steady flow computed via the solution to the flow equations. It can be observed that the Gaussian profile is a good match for the velocity profiles far downstream of the cylinder. Close to the cylinder the strong shear layer causes the profile to have sharp change in the slope. Using the computed profiles we estimate the local Reynolds number,  $Re_l$ , based on the maximum velocity defect ( $= s(x) u(x, y = H)$ ) and the wake half-width. Figure 14 shows the streamwise variation of  $s$ ,  $b$  and  $Re_l$ . The parameter  $s(x)$  is computed with the help of the expression:  $s(x) = \frac{u(x, y=H) - u(x, y=0)}{u(x, y=H)}$ . The wake half width,  $b(x)$ , is the vertical distance from the wake centerline where the velocity defect with respect to  $u(x, y = H)$  is one-half the maximum defect at each location ( $= u(x, H) - u(x, 0)$ ).

From the figure it is seen that, as expected, there is an appreciable reverse flow close to the cylinder. While  $s$  and  $b$  change to some extent, the  $Re_l$  shows substantial streamwise variation. The maximum for  $Re_l$  is slightly lower than  $45$ . The critical  $Re$  for convective instability predicted by Castro (2005) for  $H = 10$  is  $53.06$  and  $H = 100$  is  $52.99$ . Since both these values are very close one can assume the

critical for  $H = 50$  to be close to 53. The maximum value of  $Re_l$  from the present analysis is lower ( $\sim 45$ ). This value is achieved in the near wake of the cylinder. As seen from Figure 13, in this region, the velocity profiles for the base flow from the direct numerical simulations are quite different than the Gaussian profile utilized by Castro (2005). Therefore, a difference in the results from the two methods is not surprising. In fact, it is quite interesting that the two approaches lead to comparable values of  $Re_c$  that are different by less than 20%.

## 6 Summary & Conclusions

Global linear stability analysis of steady flow past a circular cylinder has been carried out in a frame translating in the streamwise direction. Free-slip condition at the centerline of the flow field is imposed in order to suppress the symmetric modes. Under these conditions only half the domain needs to be investigated. The steady flow for this setup represents the flow past a cascade of circular cylinders. However, the stability results are specific to the present case. For computing the steady flow various locations of the lateral boundary are considered. The results are found to be in very good agreement with those reported by other researchers (Fornberg (1985); Fornberg (1991); Gajjar and Azzam (2004)). The eddy length varies linearly with  $Re$ . Depending on the blockage, three different types of solutions with respect to the structure of the eddy, are found. For very high blockage the eddy has relatively large length compared to its width. The eddy width first increases and then decreases in the streamwise direction. For moderate blockage the eddy width is almost constant but is found to have an abrupt bulge at the reattachment point. For low blockage the bubble width is large and the effect of the confining walls is almost negligible. The computational resources required for accurate computations with low blockage are quite high. For this reason the results for the  $H = 50$  flow are restricted to  $Re = 500$ .

The linear stability analysis of the steady flow is carried out via an eigenvalue formulation to get the most unstable modes, their growth rate and the corresponding frequency. Only  $H = 50$  case is considered and perturbations are restricted to move only in the streamwise direction. Computations are done for various speeds at a given  $Re$ . The growth rate shows a nonmonotonic variation with the wave speed  $c_x$ . Over all, the growth rate increases with increase in  $Re$ . The  $St$  also shows a nonmonotonic variation with  $c_x$ , at a given  $Re$ . The critical  $Re$  for the onset of shear layer instability, from the present analysis, is found to be 54. The linear stability analysis for the  $Re = 500$  flow leads to three kinds of modes depending on the speed of the disturbance. Based on the vortical structures in the modes they are classified as the bubble, shear layer and tornado modes.

The present results from the linear stability analysis are also supported by those

from direct time integration of linearized disturbance equations. The time evolution of the energy of the disturbance shows intermediate increase upto very high values before decaying. Such large increase in energy has also been observed earlier for other flow problems (Fasel and Postl (2006)). This suggests that very small sustained background disturbances can grow to significant strength and be observed in a flow. They can, erroneously, give the same effect as a global absolute instability. Time integration of the nonlinear disturbance equation also shows the appearance of the modes obtained from linear stability analysis.

The results from the global analysis are compared with earlier results from local analysis (Hultgren and Aggarwal (1987) and Castro (2005)). For the  $Re_c$  from the global analysis, the streamwise variation of the local Reynolds number ( $Re_l$ ), based on the maximum speed difference and the wake half width, is determined for the base flow.  $Re_l$  shows substantial streamwise variation and achieves a maximum value which is a little less than 45. The local analysis predicts about 20% lower value. This difference might also be because the local analysis by Castro (2005) and Hultgren and Aggarwal (1987) was carried out for a synthetic velocity profile based on a Gaussian distribution. In the near wake the velocity profile from the present analysis are different from the Gaussian profile. However, they are in very good agreement in the far wake.

It may be pointed out that although the present work has been restricted to the investigation of convective instability of the steady flow, the same analysis for the time-averaged flow can also reveal useful information. This might be especially relevant in the case of high  $Re$  flows. Recently Mittal (2008a,b) showed that the global absolute stability analysis of the time averaged flow past a circular cylinder predicts the correct Strouhal frequency of the fully nonlinear flow.

**Acknowledgement:** Partial support for this work from the Department of Science & Technology, India is gratefully acknowledged.

## References

**Atluri, S.; Han, Z.; Rajendran, A.** (2003): A new implementation of the meshless finite volume method, through the MLPG mixed approach. *CMES: Computer Modeling in Engineering and Sciences*, vol. 4, pp. 507–517.

**Atluri, S.; Shen, S.** (2002): The meshless local Petrov-Galerkin (MLPG) method: A simple and less-costly alternative to the finite element and boundary element methods. *CMES: Computer Modeling in Engineering and Sciences*, vol. 3, pp. 11–51.

**Atluri, S.; Zhu, T.** (1998): A new meshless local Petrov-Galerkin approach in computational mechanics. *Computational Mechanics*, vol. 22, pp. 117–127.

**Atluri, S.; Zhu, T.** (2000): New concepts in meshless methods. *International Journal For Numerical Methods In Engineering*, vol. 47, pp. 537–556.

**Belytschko, T.; Organ, D.; Y.Krongauz** (1994): A coupled finite element-free Galerkin method. *International Journal For Numerical Methods In Engineering*, vol. 17, pp. 186–195.

**Bers, A.** (1983): In Rosenbluth, M. N.; Sagdeev, R.(Eds): *Handbook of Plasma Physics*, volume 1, pp. 451–517. North-Holland, New York.

**Briggs, R. J.** (1964): *Electron Stream Interaction with Plasmas*. MIT Press, Cambridge, MA.

**Brooks, A. N.; Hughes, T. J. R.** (1982): Streamline upwind/Petrov-Galerkin formulations for convection dominated flows with particular emphasis on the incompressible Navier-Stokes equations. *Computer Methods in Applied Mechanics and Engineering*, vol. 32, pp. 199–259.

**Castro, I. P.** (2005): The stability of laminar symmetric separated wakes. *Journal of Fluid Mechanics*, vol. 532, pp. 389–411.

**Chen, J. H.; Pritchard, W. G.; Tavener, S. J.** (1995): Bifurcation for flow past a cylinder between parallel planes. *Journal of Fluid Mechanics*, vol. 284, pp. 23–41.

**Chomaz, J. M.; Huerre, R.; Redekopp, L. G.** (1988): Bifurcations to local and global modes in spatially developing flows. *Physical Review Letters*, vol. 60, pp. 25–28.

**Ding, Y.; Kawahara, M.** (1999): Three dimensional linear stability analysis of incompressible viscous flows using the finite element method. *International Journal for Numerical Methods in Fluids*, vol. 31, pp. 451–479.

**Dizes, S. L.; Huerre, P.; Chomaz, J. M.; Monkewitz, P. A.** (1996): Linear global modes in spatially developing media. *Philosophical Transactions of the Royal Society of London*, vol. 354, pp. 169–212.

**Fasel, H. F.; Postl, D.** (2006): Interaction of separation and transition in boundary layers: Direct numerical simulations. In *Sixth IUTAM Symposium on Laminar-Turbulent Transition*, pp. 71–88, Springer.

**Fornberg, B.** (1985): Steady viscous flow past a circular cylinder up to Reynolds number 600. *Journal of Computational Physics*, vol. 98, pp. 297–320.

**Fornberg, B.** (1991): Steady incompressible flow past a row of circular cylinders. *Journal of Fluid Mechanics*, vol. 225, pp. 655–671.

**Gajjar, J. S. B.; Azzam, N. A.** (2004): Numerical solution of the Navier-Stokes equations for the flow in a cylinder cascade. *Journal of Fluid Mechanics*, vol. 520, pp. 51–82.

**Huerre, P.; Monkewitz, P. A.** (1985): Absolute and convective instabilities in free shear layers. *Journal of Fluid Mechanics*, vol. 159, pp. 151–168.

**Huerre, P.; Monkewitz, P. A.** (1990): Local and global instabilities in spatially developing flows. *Annu. Rev. Fluid Mech.*, vol. 22, pp. 473–537.

**Hughes, T.; Franca, L.; Balestra, M.** (1986): A new finite element formulation for computational fluid dynamics: V. Circumventing the Babuška–Brezzi condition: A stable Petrov–Galerkin formulation of the Stokes problem accommodating equal-order interpolations. *Computer Methods in Applied Mechanics and Engineering*, vol. 59, pp. 85–99.

**Hughes, T. J. R.; Brooks, A. N.** (1979): A multi-dimensional upwind scheme with no crosswind diffusion. In Hughes, T.(Ed): *Finite Element Methods for Convection Dominated Flows*, AMD-Vol.34, pp. 19–35. ASME, New York.

**Hultgren, L. S.; Aggarwal, A. K.** (1987): Absolute instability of the gaussian wake profile. *Physics of Fluids*, vol. 30, pp. 3383–3387.

**Jackson, C. P.** (1987): A finite-element study of the onset of vortex shedding in flow past variously shaped bodies. *Journal of Fluid Mechanics*, vol. 182, pp. 23–45.

**Koch, W.** (1985): Local instability characteristics and frequency determination of self-excited wake flows. *Journal of Sound and Vibration*, vol. 99, pp. 53–83.

**Kumar, B.; Kottaram, J. J.; Singh, A. K.; Mittal, S.** (2009): Global stability of flow past a cylinder with centreline symmetry. *Journal of Fluid Mechanics*, vol. 632, pp. 273–300.

**Kumar, B.; Mittal, S.** (2006): Effect of blockage on critical parameters for flow past a circular cylinder. *International Journal for Numerical Methods in Fluids*, vol. 50, pp. 987–1001.

**Kumar, B.; Mittal, S.** (2006): Prediction of the critical Reynolds number for flow past a circular cylinder. *Computer Methods in Applied Mechanics and Engineering*, vol. 195, pp. 6046–6058.

**Landau, L. D.; Lifshitz, E. M.** (1959): *Fluid Mechanics*. Pergamon Press, Oxford.

**Lin, H.; Atluri, S.** (2002): Meshless local Petrov-Galerkin (MLPG) method for convection-diffusion problems. *CMES: Computer Modeling in Engineering and Sciences*, vol. 1, pp. 45–60.

- Liu, W.; Chen, Y.; Chang, C.; Belytschko, T.** (1996): Advances in multiple scale kernel particle methods. *Computational Mechanics*, vol. 18, pp. 73–111.
- Mittal, S.** (2008): Global linear stability analysis of time-averaged flows. *International Journal for Numerical Methods in Fluids*, vol. 58, pp. 111–118.
- Mittal, S.** (2008): Linear stability analysis of time-averaged flow past a cylinder. *CMES: Computer Modeling in Engineering and Sciences*, vol. 27, pp. 63–78.
- Mittal, S.; Kottaram, J. J.; Kumar, B.** (2008): Onset of shear layer instability in flow past a cylinder. *Physics of Fluids*, vol. 20, pp. 054102–1–10.
- Mittal, S.; Kumar, B.** (2007): A stabilized finite element method for global analysis of convective instabilities in nonparallel flows. *Physics of Fluids*, vol. 19, pp. 088105–1–4.
- Mohammadi, M. H.** (2008): Stabilized meshless local petrov-galerkin (mlpg) method for incompressible viscous fluid flows. *CMES: Computer Modeling in Engineering and Sciences*, vol. 29, pp. 75–94.
- Monkewitz, P. A.; Huerre, P.; Chomaz, J. M.** (1993): Global linear stability analysis of weakly non-parallel shear flows. *Journal of Fluid Mechanics*, vol. 251, pp. 1–20.
- Morzynski, M.; Afanasiev, K.; Thiele, F.** (1999): Solution of the eigenvalue problems resulting from global non-parallel flow stability analysis. *Computer Methods in Applied Mechanics and Engineering*, vol. 169, pp. 161–176.
- Norberg, C.** (1994): An experimental investigation of the flow around a circular cylinder: influence of aspect ratio. *Journal of Fluid Mechanics*, vol. 258, pp. 287–316.
- Norberg, C.** (2001): Flow around a circular cylinder: aspects of fluctuating lift. *Journal of Fluids and Structures*, vol. 15, pp. 459–469.
- Pierrehumbert, R. T.** (1984): Local and global baroclinic instability of zonally varying flow. *Journal of the Atmospheric Sciences*, vol. 41, pp. 2141–2162.
- Saad, Y.; Schultz, M.** (1986): GMRES: A generalized minimal residual algorithm for solving nonsymmetric linear systems. *SIAM Journal of Scientific and Statistical Computing*, vol. 7, pp. 856–869.
- Sadovskii, V.** (1971): On local properties of vortex flows. *Uch. Zap. TsAGI*, vol. 4, pp. 117–120.
- Smith, F.** (1979): Laminar flow of an incompressible fluid past a bluff body: the separation, reattachment, eddy properties and drag. *Journal of Fluid Mechanics*, vol. 92, pp. 171–205.

**Tezduyar, T. E.; Mittal, S.; Ray, S. E.; Shih, R.** (1992): Incompressible flow computations with stabilized bilinear and linear equal-order-interpolation velocity-pressure elements. *Computer Methods in Applied Mechanics and Engineering*, vol. 95, pp. 221–242.

**Williamson, C. H. K.** (1989): Oblique and parallel modes of vortex shedding in the wake of a circular cylinder at low Reynolds numbers. *Journal of Fluid Mechanics*, vol. 206, pp. 579–627.

**Zebib, A.** (1987): Stability of viscous flow past a circular cylinder. *J.Engrg.Math.*, vol. 21, pp. 155–165.

**Zhu, T.; Zhang, J.; Atluri, S.** (1998): A local boundary equation (LBIE) approach in computational mechanics and a meshless discretization approach. *Computational Mechanics*, vol. 21, pp. 223–235.

